nature catalysis

ARTICLES

https://doi.org/10.1038/s41929-022-00751-0

Check for updates

Highly selective and productive reduction of carbon dioxide to multicarbon products via in situ CO management using segmented tandem electrodes

Tianyu Zhang[1,4], Justin C. Bui[2,3,4], Zhengyuan Li[1], Alexis T. Bell[2,3], Adam Z. Weber[3]✉ and Jingjie Wu[1]✉

Electrochemical CO_2 reduction provides a promising route to the sustainable generation of valuable chemicals and fuels. Tandem catalysts enable sequential CO_2-to-CO and CO-to-multicarbon (C_{2+}) product conversions on complementary active sites, to produce high C_{2+} Faradaic efficiency (FE). Unfortunately, previous tandem catalysts exhibit poor management of CO intermediates, which diminishes C_{2+} FE. Here, we design segmented gas-diffusion electrodes (s-GDEs) in which a CO-selective catalyst layer (CL) segment at the inlet prolongs CO residence time in the subsequent C_{2+}-selective segment, enhancing conversion. This phenomenon enables increases in both the CO utilization and C_{2+} current density for a Cu/Ag s-GDE compared to pure Cu, by increasing the *CO coverage within the Cu CL. Lastly, we develop a Cu/Fe-N-C s-GDE with 90% C_{2+} FE at C_{2+} partial current density (j_{C2+}) exceeding 1 A cm^{-2}. These results prove the importance of transport and establish design principles to improve C_{2+} FE and j_{C2+} in tandem CO_2 reduction.

The electrochemical reduction of CO_2 (CO_2R) to value-added chemicals utilizing renewable energy provides a sustainable route to the generation of fuels and chemicals while simultaneously mitigating CO_2 emissions[1,2]. Of the products that can be generated from CO_2R, multicarbon (C_{2+}) products are the most desirable due to their industrial value as a chemical feedstock[3,4]. Among the catalysts explored for CO_2R, only Cu-containing materials have demonstrated the capacity to generate C_{2+} products, and many previous studies have aimed to develop catalysts exhibiting enhanced rates for C_{2+} generation. In the reaction of CO_2 to C_{2+} on Cu, the kinetics of the rate-determining step, which dictates the partial current density for C_{2+} products (j_{C2+})[5–9], depends on the adsorption energy of adsorbed carbon monoxide (*CO) and, subsequently, on the *CO surface coverage (θ_{*CO})[10–12]. Therefore, recent work has attempted to increase the binding of *CO on Cu to increase the rate of conversion to C_{2+}[6,13–16]. Since θ_{*CO} is determined by the concentration of CO near the catalyst, the yield of C_{2+} products on Cu can be enhanced by increasing local CO concentration[12,17]. In particular, for vapour-fed systems that do not suffer from the concern of low CO solubility in the electrolyte, an increase in CO partial pressure has been shown to directly result in enhanced C_{2+} production[18].

Cascade CO_2R systems, which integrate two consecutive steps of CO_2-to-CO and CO-to-C_{2+} on two distinct catalytic sites, can intensify the θ_{*CO} on a Cu surface[19–23]. In these systems, one catalyst material selectively converts CO_2 to CO to provide an in situ source of CO that enhances θ_{*CO}, and another Cu-containing catalyst performs C–C coupling. The state-of-the-art bimetallic tandem catalysts, such as Cu/Ag and Cu/FeTPP[Cl], exhibit substantially reduced overpotential, enhanced Faradaic efficiency (FE) to C_{2+} (~85%) and improved C_{2+} partial current density (j_{C2+} = ~300 mA cm^{-2}) relative to pure Cu catalysts[24,25]. Since the θ_{*CO} is often the limiting factor, higher j_{C2+} values can be achieved by increasing the local CO partial pressure (P_{CO}) with increased CO generation rates[12,26,27]. However, if the rate of CO generation exceeds the rate of C–C coupling, CO utilization and C_{2+} FE are diminished[20,22,25,28]. This trade-off presents a need to manage in situ CO formation to maximize the C_{2+} FE while still maintaining high j_{C2+}[29,30].

Our previous studies have demonstrated the value of a layered gas-diffusion electrode (l-GDE) structure, in which a CO-selective catalyst layer (CL) is placed on top of a C_{2+}-selective Cu CL[29,30]. The l-GDE was inspired by the higher reactant conversion in a plug-flow reactor (PFR) compared to that in a continuous-stirred-tank reactor (CSTR) for reactions with a positive reaction order[31]. In a PFR, this enhancement in conversion results from increased residence time within the reactor. By creating a layered CL structure, it is possible to concentrate the CO at the CL/electrolyte interface and dimerize CO progressively along the through-plane direction of the GDE, imitating the reactant concentration profile in a PFR. This layered structure intensifies the local θ_{*CO} within the Cu CL and boosts j_{C2+} by a factor of 1.2 compared to that for a pure Cu GDE[30]. Unfortunately, the l-GDE only controls the P_{CO} profile along the through-plane direction at the micrometre scale and fails to manage the P_{CO} profile along the electrode length direction at the centimetre scale. Consequently, there is an opportunity for further enhancement of θ_{*CO} and j_{C2+}.

Here, we present a segmented gas-diffusion electrode (s-GDE) structure for selective CO_2R to C_{2+}. The s-GDE integrates a CO-selective CL segment at the inlet end of the GDE and a Cu CL segment down the rest of the GDE, enabling spatial management of θ_{*CO} in-plane along the length of the electrode. The P_{CO} is enhanced

[1]Department of Chemical and Environmental Engineering, University of Cincinnati, Cincinnati, OH, USA. [2]Department of Chemical and Biomolecular Engineering, University of California Berkeley, Berkeley, CA, USA. [3]Joint Center for Artificial Photosynthesis, Lawrence Berkeley National Laboratory, Berkeley, CA, USA. [4]These authors contributed equally: Tianyu Zhang, Justin C. Bui. ✉e-mail: azweber@lbl.gov; jingjie.wu@uc.edu

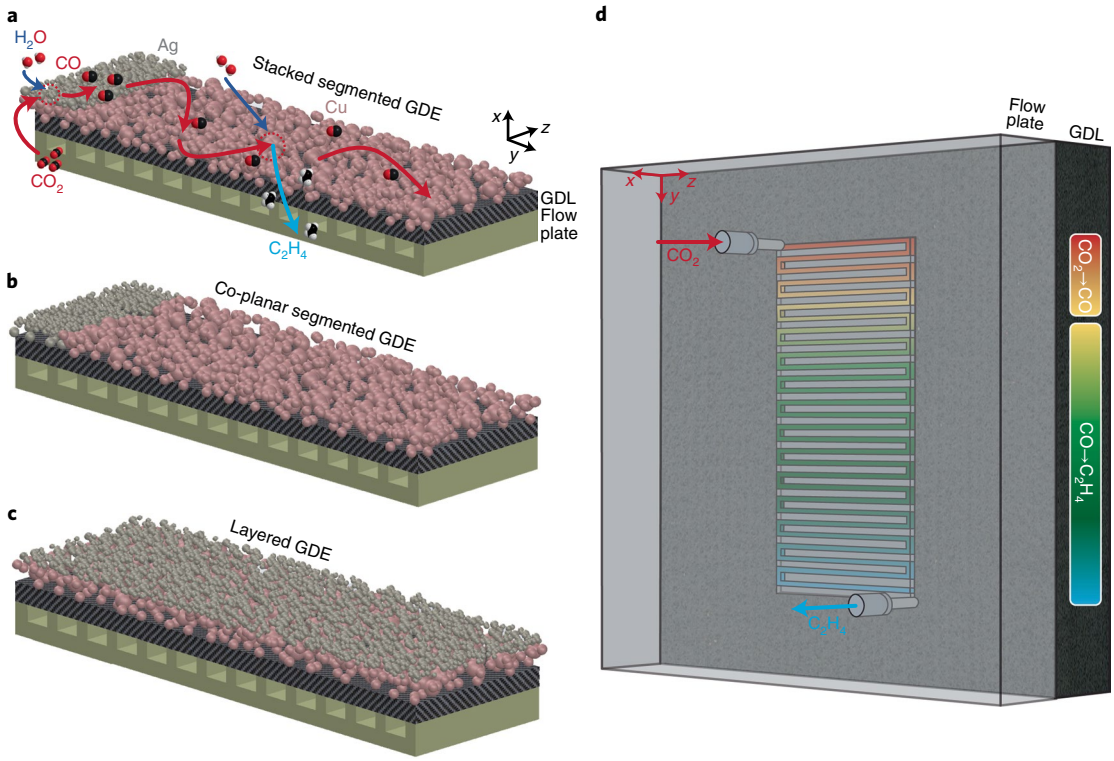

Fig. 1 | Concept of segmented tandem gas-diffusion electrodes. a–c, Schematic of stacked (**a**) and coplanar (**b**) segmented gas-diffusion electrodes. For comparison, the structure of the layered gas-diffusion electrode is also displayed in the bottom panel (**c**). The arrows in **a** represent the reaction and mass transport of the proposed tandem reaction process in the catalyst layer. **d**, Schematic of the flow-channel geometry and gas concentration changing along the flow channel during the tandem reaction of $CO_2 \rightarrow CO \rightarrow C_2H_4$.

at the inlet area, and meanwhile the CO residence time is maximized, leading to concurrently enhanced overall C_{2+} FE and j_{C2+}. The mapping of CO_2 R performance down the length of the electrode and the multiphysics modelling further prove the intimate correlation between the P_{CO} and j_{C2+}, showing that the j_{C2+} achieves a maximum at the inlet area and gradually decays with the consumption of CO generated on the CO-selective catalyst (that is, declining P_{CO}). Based on the insights gained and to prove their universality, we developed an s-GDE consisting of Cu and single-atom iron (Fe-N-C) CL segments capable of achieving 90% C_{2+} FE at j_{C2+} exceeding 1 A cm^{-2}. This work provides an in-depth understanding of design principles of tandem electrodes that simultaneously enhance selectivity and productivity towards C_{2+} products.

Results

Design of the s-GDE. Two structures of s-GDEs (stacked and coplanar) comprising Ag and Cu CL segments were designed, as shown in Fig. 1a,b. In the stacked configuration, the Cu and Ag CL segments are present in distinct layers in both the length (*y* axis) and through-plane (*z* axis) directions. In the coplanar configuration, the Cu and Ag CL segments are in a single layer in the *z* direction but are still distinct in the *y* direction. In both cases, the Ag CL segment aligns with the CO_2 gas inlet to enable rapid conversion of the incoming CO_2 into a supplementary CO supply that enhances the θ_{*CO} and can be converted to C_{2+} products over the subsequent Cu CL segment (analogous to reactant conversion in a PFR) (Fig. 1d).

Along-the-channel conversion of generated CO in a s-GDE. To understand the relationship between the P_{CO} and the rate of CO conversion, we performed a series of experiments that enabled tracking of the local P_{CO} and the j_{C2+} within individual segments along the length (*y* direction) of the s-GDE. Using the stacked s-GDE as a model geometry, the change of the local P_{CO} and C_{2+} productivity along the *y* axis was mapped indirectly by measuring the CO outflow rate and the j_{C2+} from six modified s-GDEs (see Methods for details). The resulting modified s-GDEs (E1 to E6) are 0.50 cm wide and possess a condensed 0.2 cm long Ag CL stacked on top of a Cu CL that varies from 0.2 (E1) to 2.0 cm (E6) (Fig. 2a). CO_2R performance of these six electrodes (E1 to E6) was evaluated in a membrane-electrode-assembly (MEA) electrolyser (see Methods for details).

By plotting the FE enhancements observed by extending the length of the Cu CL (Fig. 2c and Supplementary Fig. 1), it is observed that as the Cu CL segment is extended from E1 to E6, the FE to CO gradually declines from 65.5 to 6.2%, while the overall FE of C_{2+} products rises from 33.2 to 82.0%. The FE to a specific C_{2+} product (C_2H_4, C_2H_5OH, CH_3COO^- and C_3H_7OH) exhibits similar behaviour to the overall C_{2+} FE (Supplementary Fig. 4). This trend indicates that as the Cu CL is extended, the residence time of CO (generated within the Ag CL) increases within the Cu CL thereby enabling better conversion to C_{2+} products. However, the FE gradient ($|\Delta FE/\Delta L|$) of both CO and C_{2+} products declines as the Cu CL length increases, indicating that there is a length beyond which no further FE enhancements are observed because all the in situ-generated CO has been consumed. This theory is further corroborated by plotting the CO utilization, defined as the percentage of CO generated within the s-GDE that is converted to C_{2+} products (Supplementary Note 1) as a function of the Cu CL length. As shown in Fig. 2d, as the Cu CL length increases, the CO utilization towards C_{2+} formation increases, achieving a maximum value of 0.82.

To understand the enhancements in conversion, it is critical to understand the profile of the P_{CO} and C_{2+} mass activity (defined as the partial current for C_{2+} products normalized by the mass loading of Cu in the catalyst layer) within the modified s-GDE. The C_{2+}

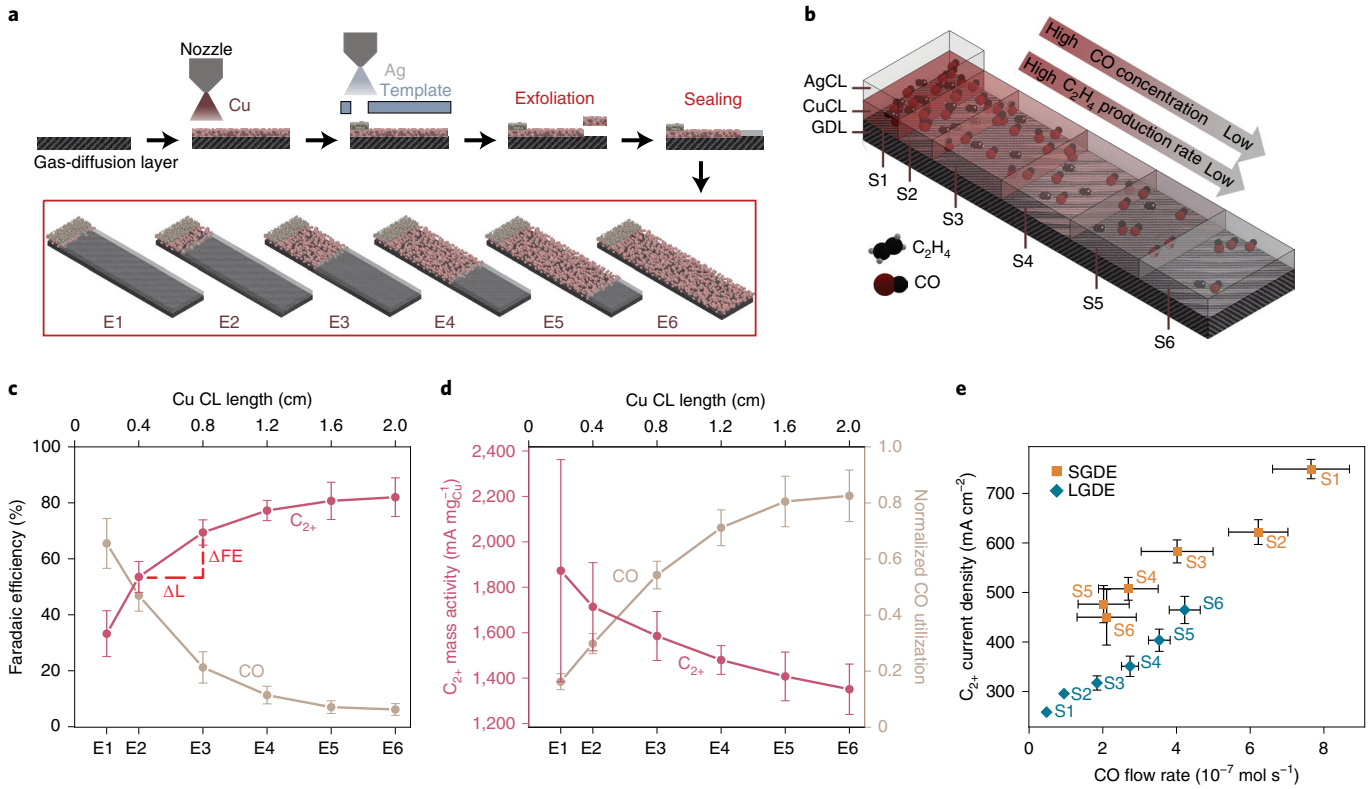

Fig. 2 | Along-the-channel conversion of generated CO in a s-GDE. a, Schematic of the s-GDE preparation procedure. The geometries of six s-GDEs (from E1 to E6) with a constant dimension of the Ag CL (L: 0.20 cm, W: 0.50 cm) and a varied dimension of the Cu CL (L: 0.20~2.00 cm, W: 0.50 cm) are shown in the inset. **b**, Schematic of decreasing C_{2+} mass activity, along with the decreasing CO concentration along the *y* axis of s-GDE. **c**, FE to CO (light brown) and C_{2+} products (dark red) versus the Cu CL length at a cathodic potential of −0.70 V versus reversible hydrogen electrode (RHE), calculated by subtracting the anode potential from the IR-corrected applied cell voltage (Supplementary Figs. 2 and 3). **d**, CO utilization towards C_{2+} formation (light brown curve) and C_{2+} mass activity (dark red curve) versus the Cu CL length. **e**, Local j_{C2+} plotted against local CO outflow rate in the six subsegments (S1 to S6) of the s-GDE and l-GDE. The subsegment S*i* represents the difference of two Cu CL segments in two consecutive electrodes (for example, S1 = E1; S*i* = E*i* − E(*i* − 1), 6 ≥ *i* ≥ 2) and is labelled in **b**. The error bars represent the standard deviation from the measurement of three independent electrodes. C_{2+} current measured is primarily toward the generation of C_2H_4 and C_2H_5OH (Supplementary Fig. 4).

mass activity decreases as the Cu CL length increases and more CO is converted to C_{2+} products (Fig. 2d). Therefore, the conversion of in situ-generated CO to C_{2+} leads to a decay in P_{CO} down the length of the s-GDE (depicted in Fig. 2b). The corresponding decrease in mass activity to C_{2+} products as the electrode length increases also suggests that j_{C2+} is largely dependent on the local concentration of CO, rather than the local concentration of fed CO_2, which, due to the high stoichiometry of the feed gas (~10 times the amount of CO_2 required to achieve stoichiometric conversion at 1 A cm^{-2} of CO_2R), will be relatively constant throughout the s-GDE[32,33]. It is important to note that the electrochemically active surface area (ECSA) increases linearly with the Cu CL length (Supplementary Fig. 5). Therefore, the increase in ECSA alone upon extending the Cu CL is insufficient to explain the non-linear trends observed for the CO and C_{2+} partial current densities (Supplementary Fig. 4), providing further evidence that the enhanced residence time of in situ-generated CO in the extended Cu CL enables improved θ_{*CO} and thus j_{C2+}. It is noteworthy that while there is probably a large amount of CO generated in the Cu CL (Supplementary Fig. 6 and Supplementary Note 2), it appears that the trends in j_{C2+} are largely driven by the residence time of the in situ-generated CO. Placing the CO-selective catalyst at the inlet of the s-GDE leverages the along-the-channel transport within the MEA to distribute and subsequently further reduce the generated CO from the Ag. However, for the l-GDE, the in situ-generated CO can more easily exit the Cu CL before conversion.

To elucidate further the interplay between the local P_{CO} and the rate of C_{2+} generation in the s-GDE, the local CO flow rate was plotted versus j_{C2+} for each subsegment, as shown in Fig. 2e (see Methods for details). The subsegment S*i* is defined as the difference of the Cu CL segments between two consecutive electrodes, and all subsegments are labelled schematically in Fig. 2b. The gas feedstock flows from S1 to S6. The local CO flow rate in Fig. 2e represents the outlet flow rate for the full electrode E*i*, which is indicative of the local CO flow rate and the P_{CO} in each subsegment S*i*. Because these flow rates represent the outlet flow rates exiting from the last segment in each electrode, the CO flow rates measured here consist only of the CO generated in the s-GDE that is not consumed to form C_{2+} products. Most of the generated CO in these tandem electrodes is consumed to form C_{2+} products, explaining the low calculated outlet CO flow rates.

The local CO flow rate gradually decreases by 73% from S1 to S6 in the s-GDE due to the CO consumption. As expected, this decline is accompanied by the decrease of j_{C2+} from 749.2 (S1) to 450.0 mA cm^{-2} (S6). Nonetheless, while the j_{C2+} decreases from S1 to S6, the FE to C_{2+} products increases from S1 to S6. This apparent contradiction can be explained as follows. Because of the large source of supplemental CO from the Ag catalyst, S1 possesses the highest local CO concentration and thus the largest C_{2+} current density. However, as discussed previously, most of the CO in S1 is not properly utilized. Therefore, even though this segment generates a substantial amount of CO, a substantial amount of that CO

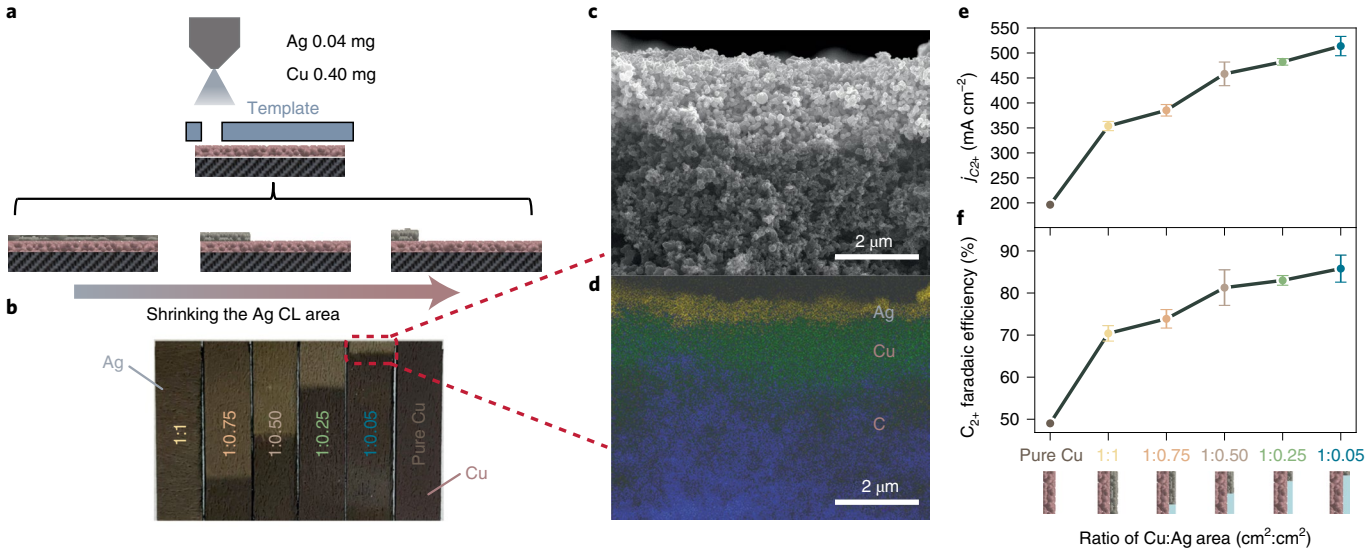

Fig. 3 | Effect of Cu:Ag area ratio on the performance of s-GDEs for CO_2 reduction. a, The schematic of the preparation procedure of five s-GDEs with fixed quantities of Cu and Ag catalysts but a varied area ratio between Cu and Ag CLs. **b**, Photographs of five Cu/Ag (*x*:*y*) s-GDEs and a control Cu GDE. *x* and *y* represent the area of the Cu and Ag CLs, respectively. **c**,**d**, The cross-sectional SEM image (**c**) and EDS elemental mapping (**d**) of the overlapping section in the Cu/Ag (1.00:0.05) s-GDE. **e**,**f**, The j_{C2+} (**e**) and C_{2+} Faradaic efficiency (**f**) as a function of the ratio of the Cu:Ag CL areas at a constant applied cell voltage of 3.05 V. The error bars represent the standard deviation from the measurement of three independent electrodes.

exits the segment before it is converted to C_{2+} products, explaining the low C_{2+} FE and high CO FE.

When performing the same analysis of the relationship between local CO flow rate and C_{2+} productivity in subsegments of l-GDEs (see Methods for details), similar behaviour is observed. These modified l-GDE electrodes (E1 to E6) possess stacked Ag and Cu CLs of equal length that vary from 0.20 cm (E1) to 2.00 cm (E6) (Supplementary Figs. 7–9) with the Ag and Cu mass of E6 for the l-GDE and s-GDE being equivalent. As the CO flow rate in the l-GDE increases, the j_{C2+} increases at a rate identical to that of the s-GDE, with both the plots of the s-GDE and l-GDE CO flow rates versus C_{2+} current densities possessing linear slopes of 5×10^9 C m^{-2} mol^{-1}. The fact that the trend of the subsegment j_{C2+} exhibits a linear relationship with the local CO flow rate supports our hypothesis that the C_{2+} production rate depends primarily on P_{CO}. However, it is important to note that at an equivalent CO flow rate, the l-GDE possesses lower C_{2+} current density than the s-GDE, which is due to differences in the in situ CO management along the *y* axis. Due to the more PFR-like nature of the s-GDE, the residence time, and thus the rate of conversion, is higher for the s-GDE than for the l-GDE, even for equivalent CO flow rates. The enhanced concentration of CO and θ_{*CO} in the s-GDE structure promotes greater j_{C2+}.

Effect of Cu:Ag area ratio on s-GDEs for CO_2 reduction. To further assess the impact of the spatial management of CO concentration on the rate of C_{2+} production within s-GDEs, five different stacked Cu/Ag s-GDEs with varying ratios of Cu and Ag CL areas were prepared and tested. The area of the Cu CL was held at 1.00 cm^2, while the Ag CL had the same width, but its length was varied from 0.10 cm to 2.00 cm (that is, its area varied from 0.05 to 1.00 cm^2) (Fig. 3a,b). These s-GDEs are denoted as Cu/Ag (*x*:*y*) s-GDE, where *x* and *y* represent the area of the Cu and Ag CLs, respectively. A pure Cu GDE was also prepared for comparison. The mass of Cu was maintained at 0.40 mg while the corresponding Ag mass was optimized to maximize CO utilization rates and kept the same for all s-GDEs (Supplementary Fig. 10). Because the Ag mass is kept constant for all Ag CL areas, the thickness of the Ag CL segment grows as its area shrinks. Figure 3c,d shows the cross-sectional scanning electron microscopy (SEM) and energy-dispersive spectroscopy (EDS) of the overlapping section of the two CLs in the Cu/Ag (1.00:0.05) s-GDE, which has the thickest Ag CL in this study. The total thickness of the CL in the overlapping area is ~2.0 μm, including 0.5 μm for the Ag CL, which is still thin enough so as not to produce mass-transport limitations, in accordance with our previous work[29,30].

As shown in Fig. 3e,f, all s-GDEs offer an improved yield of C_{2+} products compared to the Cu GDE at an equivalent applied cell voltage. The product distributions, total current densities and partial current density of C_{2+} products for all tested GDEs are shown in Supplementary Figs. 11 and 12. For the s-GDEs, both the FE of C_{2+} products (Fig. 3f) and j_{C2+} (Fig. 3e) rise gradually as the Ag CL area shrinks from 1.00 cm^2 to 0.05 cm^2. The Cu/Ag (1.00:0.05) s-GDE exhibits the highest C_{2+} FE and j_{C2+} because it produces the highest concentration of CO and, in accordance with the results shown in Fig. 2, achieves the highest CO utilization. The Cu/Ag (1.00:0.05) s-GDE achieves a maximum FE of C_{2+} of 86.1% and j_{C2+} of 559.5 mA cm^{-2} at a cell voltage of 3.16 V. The cell voltage reported here is IR compensated unless otherwise stated. The internal cell resistance varies with different contact resistances and membrane ionic resistance. IR compensation enables a more rigorous comparison of the kinetic performance between different tandem electrodes by deconvoluting the variable effects of cell assembly and membrane conductivity. Moreover, the electrochemical testing used a strong alkaline anolyte (0.5 M KOH) to reduce the applied overpotential. Therefore, the cell voltages reported here are only for comparison with devices operated in similar conditions with IR correction. Nonetheless, these values correspond to a 1.7× increase in C_{2+} FE and a 2.7× increase in j_{C2+} compared to a pure Cu GDE at the same applied cell voltage. Supplementary Fig. 13 shows that the yields of C_2H_4 and C_2H_5OH as a function of Ag CL area follow similar trends. Notably, all s-GDEs exhibit lower FE and partial current density of CO than the Cu GDE (Supplementary Fig. 14), which translates to a greater CO utilization. Furthermore, the residence time of the in situ-generated CO was estimated for each s-GDE (Supplementary Note 3), demonstrating that the average residence time of the CO increases as the ratio of Cu/Ag area is increased. This

increase in the CO utilization and residence time for the s-GDE when compared to the Cu GDE implies that the increased θ_{*CO} not only allows for greater conversion of the in situ-generated CO, but also enables increased conversion of the Cu-generated *CO intermediates by mass action.

The value of θ_{*CO} along the y axis is controlled by two critical factors, the area ratio and the spatial arrangement of the Cu and Ag CL segments. The Ag layer must be placed at the inlet to exploit the along-the-channel gradients and enhance θ_{*CO}. However, the out-of-plane overlap between Cu and Ag CLs segments in the stacked s-GDE configuration is not necessarily required. Apart from the stacked Cu/Ag (1.00:0.05) s-GDE, an alternative s-GDE was prepared, which has coplanar Cu and Ag CL segments (Fig. 1b) with areas of 0.95 and 0.05 cm^2, respectively. The coplanar Cu/Ag (0.95:0.05) s-GDE exhibits comparable activity and C_{2+} FE to the stacked Cu/Ag (1.00:0.05) s-GDE (Supplementary Fig. 15). This result demonstrates that along-the-channel gradients in the y direction dominate with regard to enhancing residence time and j_{C2+} rather than through-plane transport in the z direction.

Simulation of CO mass transport and adsorption in an s-GDE. A two-dimensional (2D) continuum model of the cathodic chamber of the cell was developed to rationalize and guide the results and design, respectively. Multiple previous studies in aqueous electrolytes have shown that the generation of C_{2+} products from CO follows an approximately first-order rate dependence on CO concentration at low CO partial pressures, for which the fraction of empty Cu sites is near unity[2,9,26,34–38]. This rate order is consistent with the linear trends observed in Fig. 2e and is consistent with previous experimental studies of CO reduction (COR)[9,12,26,30,34]. However, recent studies of vapour-phase COR have demonstrated that appreciable θ_{*CO} can be achieved in porous catalyst layers, causing the rate order with respect to CO concentration to decrease as the partial pressure increases, a behaviour captured by a Langmuir adsorption model (Supplementary Fig. 16)[12,30]. This Langmuir adsorption model was implemented in a multiphysics simulation of gas-phase CO and CO_2 transport within the s-GDE and flow channel (shown schematically in Fig. 4a) to estimate the local θ_{*CO} in experimentally tested s-GDEs (see the Supplementary Methods for a more detailed discussion). It is important to note that the simulation assumes the s-GDE behaves as a perfect tandem. In other words, all C_{2+} products are derived from CO generated over Ag, as opposed to the direct reduction of CO_2 on Cu. While indeed a simplification, this assumption is relatively consistent with the results shown in Fig. 2, which suggest that the trends in j_{C2+} are largely driven by the consumption of in situ-generated CO. Additionally, the results in Supplementary Fig. 12 demonstrate that at any given voltage, j_{C2+} is lower for the case of pure Cu GDE, thus implying that the rate of CO_2 conversion is much slower than that of CO.

As shown in Fig. 4b and Supplementary Fig. 17, moving from an l-GDE (Cu/Ag 1.00:1.00) to an s-GDE with a highly concentrated Ag layer (Cu/Ag 1.00:0.05) increases the average value of θ_{*CO} achieved within the catalyst layer. This phenomenon can be explained as follows. As the Cu:Ag area ratio increases, the formation of CO in the Ag CL occurs in a concentrated end near the inlet, thereby raising the local concentration of CO, resulting in an increased θ_{*CO} locally near the Ag/Cu boundary that decays along the length of the Cu CL as CO is consumed to form C_{2+}. This change in θ_{*CO} profile with increasing Cu/Ag area ratio is reflected in the simulations shown in Fig. 4c and is consistent with the above results. Figure 4d shows the average θ_{*CO} achieved in the CL as a function of the Cu/Ag area ratio at constant j_{C2+}, demonstrating that for the same j_{C2+}, the average θ_{*CO} in the Cu CL increases as the length of the Ag layer shrinks. This increase in the average θ_{*CO} enhances j_{C2+} by mass action and corresponds to a decrease in the required overpotential to achieve the identical C_{2+} current density, consistent with the shift in overpotential observed experimentally in Supplementary Fig. 12. The simulations provide evidence for the hypothesis that a higher average θ_{*CO} is achieved in s-GDEs.

It is important to note, however, that the simulations do not predict an increase in the average value of θ_{*CO} going from a Cu/Ag area ratio of 1.00:0.25 to 1.00:0.05, despite the enhancement in the j_{C2+} observed experimentally. This discrepancy can be rationalized as follows. First, the simulation is 2D, and does not account for in-plane transport along the width of the electrode (x direction), because these gradients are probably small due to the uniformity of the s-GDE in the x direction. However, to capture fully the enhancements going from Cu/Ag 1.00:0.25 to 1.00:0.05, it may be necessary to develop a full three-dimensional (3D) model that accounts for the serpentine flow channel. Secondly, when considering the average P_{CO} in the Cu CL as a function of the area ratio (Supplementary Fig. 18), an increase is observed from 1.00:0.25 to 1.00:0.05. The fact that the average P_{CO} continues to increase while the average θ_{*CO} does not is because the rate order with respect to P_{CO} is decreasing with increased partial pressure, and overconcentrating CO hampers CO redistribution and θ_{*CO} as simulated. This turning point is not observed experimentally, suggesting that the fit Langmuir behaviour may not be fully accurate. Nonetheless, the simulation generally agrees with and explains the experimental results.

The simulations presented here underscore the importance of optimizing the flow rate of the CO_2 feed gas in tandem catalysis. As shown in Supplementary Fig. 19, for a Cu/Ag (1.00:0.05) s-GDE there is an optimal CO_2 flow rate of ~20 sccm for which a maximum average θ_{*CO} can be achieved. This optimum feed flow rate matches that chosen for experiment and can be justified by analysis of the simulated transport of CO generated in the Ag CL of an s-GDE. The CO generated over Ag transports out of the CL and back into the flow channel. In the flow channel, the CO_2 acts as a carrier gas to provide convection of CO down the channel where it is re-distributed along the length of the Cu CL (Supplementary Fig. 20). Therefore, if the molar flow rate of the CO_2 feed is too low, there is insufficient convective flux to carry the generated CO down the length of the channel where it can be adsorbed and react on the Cu CL segment. However, for an excessively high feed rate, the CO will be preferentially swept out of the flow channel, as opposed to being re-distributed into the Cu CL. The existence of an optimum molar flow rate of CO_2 has been demonstrated in previous studies of CO_2R on Cu[21,39,40], and further demonstrates the importance of optimizing mass transport.

The compatibility between Cu and CO-selective catalysts. CO-selective catalysts, such as Ag, ZnO and emerging single-atom catalysts (for example, iron-nitrogen-carbon (Fe-N-C) nanostructure), exhibit dramatically different performance for CO evolution at a given applied voltage (Supplementary Fig. 21). The effectiveness of the s-GDE requires compatible overpotentials to produce CO in the CO-selective CL and subsequently dimerize that CO in the Cu CL. To determine the optimal catalyst pairing, we compared s-GDE performance for three CO-selective catalysts: Ag, ZnO and Fe-N-C. For fair comparison, the catalyst loading, electrode structure and spatial orientation of the Cu/ZnO and Cu/Fe-N-C s-GDEs were equivalent to those of the optimized Cu/Ag (1.00:0.05) stacked s-GDE (Fig. 1a). Fe-N-C requires the lowest overpotential for maximum C_{2+} production, followed by Ag and ZnO (Fig. 5a and Supplementary Figs. 22–24; Supplementary Fig. 22 demonstrates the full-cell voltage without IR correction). Therefore, the Cu/Fe-N-C s-GDE presents the greatest opportunity to generate C_{2+} products at low overpotential, achieving a maximum C_{2+} FE of 87.3% and j_{C2+} of 437.2 mA cm^{-2} at 2.89 V (Fig. 5a and Supplementary Fig. 23). The C_2H_4 FE accounts for 46.9% at this cell voltage (Supplementary Fig. 24).

Seeking to achieve higher j_{C2+} on the Cu/Fe-N-C s-GDE, both the Cu and Fe-N-C loadings were doubled (that is, Cu loading

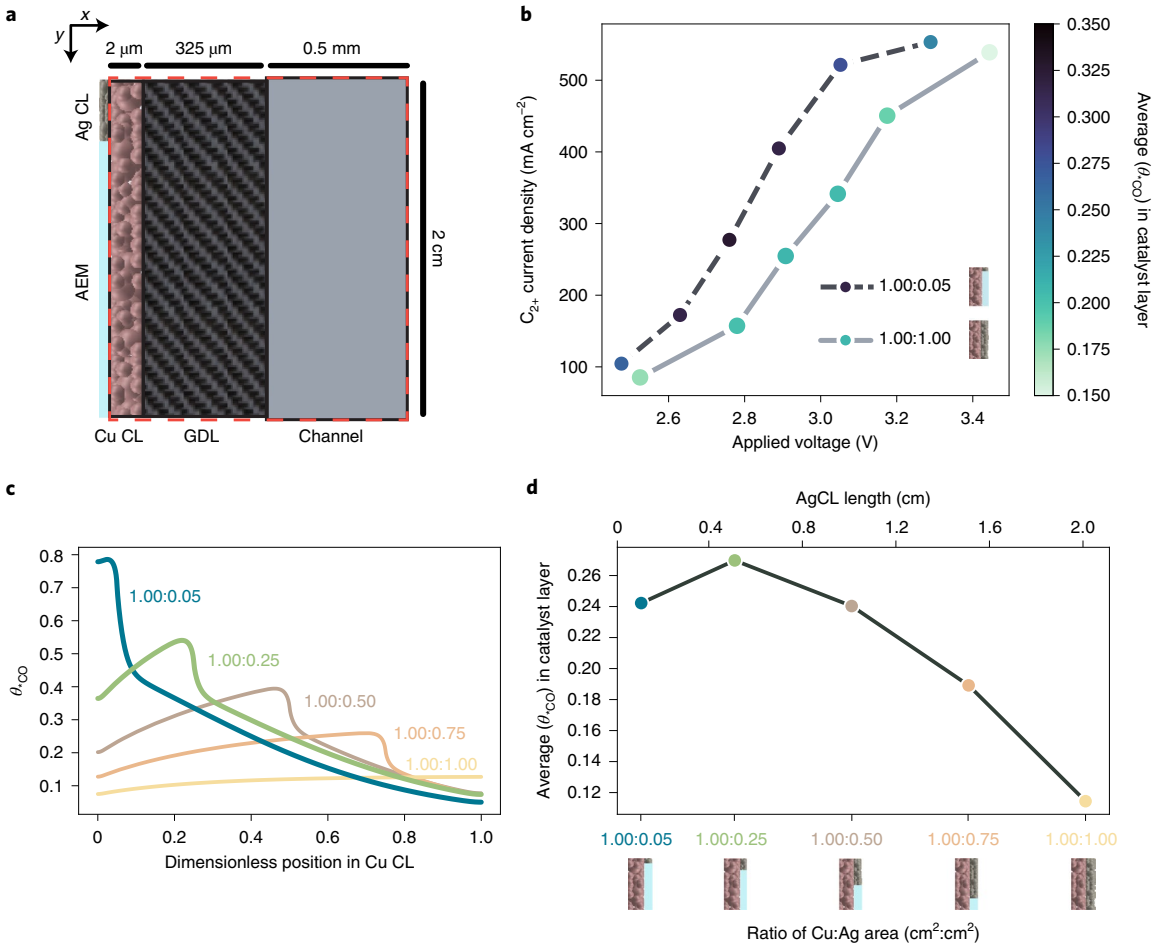

Fig. 4 | Multiphysics model of mass transport and CO adsorption in an s-GDE. a, Schematic of the modelled domain (red dotted box). **b**, Polarization curves for the Cu/Ag (1.00:0.05) s-GDE and (1.00:1.00) s-GDE. Colour of the marker represents the average *CO surface coverage attained in the Cu CL for a given Cu/Ag area ratio, voltage and C_{2+} current density. **c**, Simulated profiles of local θ_{*CO} in the Cu CL for all five Cu/Ag area ratios studied experimentally at a C_{2+} current density of 550 mA cm^{-2}. **d**, Average local θ_{*CO} in the Cu CL versus Cu/Ag area ratio at a C_{2+} current density of 550 mA cm^{-2}.

of 0.80 mg cm^{-2}). Since severe flooding resulting from enhanced electro-osmotic transport restricted the operation of the MEA electrolyser to current densities under 1,000 mA cm^{-2}, experiments with the doubly loaded Cu/Fe-N-C s-GDE were transferred to a flow cell equipped with a thin buffer layer (2 mm) in the cathodic compartment, between the membrane and the catalyst layer[41,42]. The electrolyte stream reduces the water chemical potential gradient and enables high current operation at the cost of the increased cell resistance (0.20 to ~0.60 Ω for the MEA cell versus 1.00 to ~1.10 Ω for the flow cell) (Supplementary Fig. 2). After doubling the loading, the Cu/Fe-N-C s-GDE achieves a j_{C2+} of 1071.7 mA cm^{-2} and a C_{2+} FE of 89.3% at 3.38 V (Fig. 5b–d and Supplementary Fig. 25). These values correspond to 1.8× and 1.2× increases in the j_{C2+} and C_{2+} FE, respectively, compared to those for a pure Cu GDE tested in the flow cell under identical conditions (Supplementary Fig. 26). Moreover, the C_2H_4 FE rises to 63.5% at j_{C2H4} of 761.7 mA cm^{-2}. The half-cell energy efficiency to C_2H_4 in the flow cell is 40.1%, while the full-cell energy efficiency is 16.9% due to high ohmic resistance in the cell with the thin electrolyte layer (Supplementary Fig. 27; see Methods for description of efficiency calculation).

Long-term stability and CO_2 cross-over. The flooding of the CL restricts the long-term operation at current densities exceeding 500 mA cm^{-2} in the MEA electrolyser (Supplementary Fig. 28). Therefore, the long-term durability of Cu/Fe-N-C s-GDE was assessed in the flow cell. The Cu/Fe-N-C s-GDE maintained over 80 and 60% FEs to C_{2+} products and C_2H_4, respectively, for 24 h at an operating j_{total} of 680 mA cm^{-2} (Fig. 5e). After 24 h, the j_{total} fluctuated, and the FEs to C_{2+} products and C_2H_4 decayed due to pressure build-up in the CO_2 feed, accompanied by electrolyte flowing out from the gas flow channel and, subsequently, a short supply of CO_2 reactants. Decreasing the j_{total} to 430 mA cm^{-2} prolonged durability to almost 120 h; however, the FEs to C_2H_4 (45%) and C_{2+} products (70%) were lowered (Supplementary Fig. 29).

Another challenge in the development of MEAs for CO_2R is mitigating the cross-over of the feed CO_2 through the anion-exchange membrane in the form of (bi)carbonate anions. When calculating the carbonate cross-over of the Cu/Fe-N-C s-GDE (Methods), it is observed that such cross-over consumes 22.5% of the total CO_2 feedstock. Previous work has demonstrated that the carbon cross-over can be lessened with an acidic or neutral catholyte[43,44], or by employing a bipolar membrane (BPM)[45]. The use of acidic electrolytes or BPMs is beyond and ancillary to the scope of the present work; the presented results and understandings should equally apply to any CO_2 cross-over mitigation strategy. However, to mitigate the cross-over and to provide another point of comparison between our study and the literature, CO_2 reduction with the Cu/Fe-N-C s-GDE was also performed in an MEA cell using 0.1 M $KHCO_3$ anolyte (Supplementary Fig. 30). As expected, the carbonate cross-over declines from 22.5% to 17.5% of the total, which,

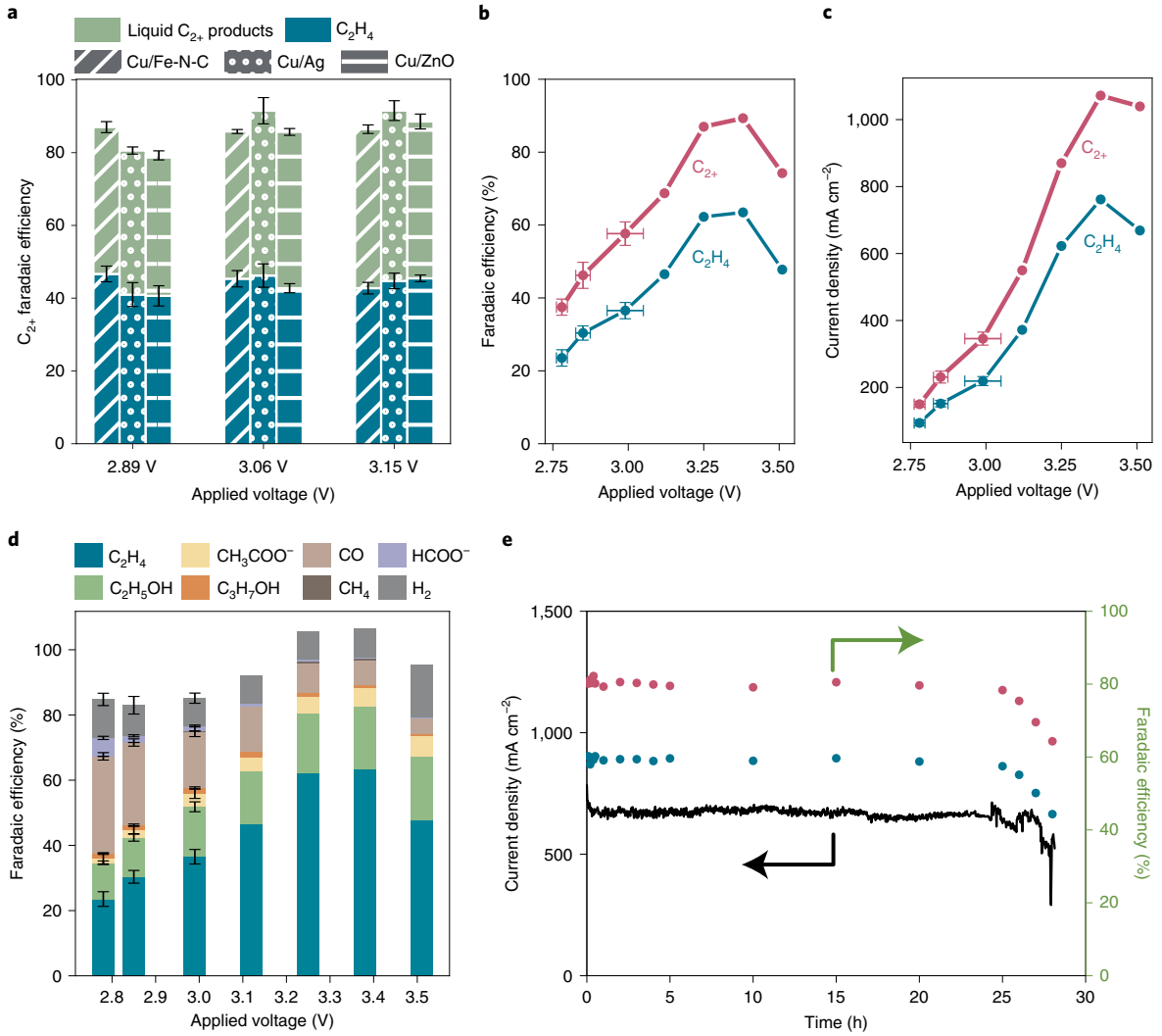

Fig. 5 | The compatibility between Cu and CO-selective catalysts. a, The Faradaic efficiency of C_2H_4 and C_{2+} liquid products for Cu/Fe-N-C, Cu/Ag and Cu/ZnO s-GDEs at three cell voltages as operated in an MEA cell. The Cu/Fe-N-C, Cu/Ag and Cu/ZnO s-GDEs achieve their optimal C_2H_4 FE at 2.89, 3.06 and 3.15 V, respectively. **b**,**c**, FE (**b**) and partial current densities (**c**) of C_2H_4 and C_{2+} products as a function of cell voltage on doubly loaded Cu/Fe-N-C s-GDE as conducted in a flow cell with a thin 0.5 M KOH layer of 2 mm. **d**, Full product distribution of doubly loaded Cu/Fe-N-C s-GDE. **e**, Long-term stability of Cu/Fe-N-C s-GDE operated in a thin buffer flow cell at 3.40 V. The error bars represent the standard deviation from measurements of at least three independent electrodes.

while not a substantial suppression of the cross-over, is a marked improvement. However, the achievable current density also declines compared to that observed for 0.5 M KOH due to increased ohmic resistance through the membrane and higher kinetic overpotentials for CO_2R at the cathode and oxygen evolution reaction at the anode[46]. Nevertheless, the performance remains quite competitive with previous studies in 0.1 M $KHCO_3$ electrolyte (Supplementary Table 4), showing the generality of the findings. Future work should seek to employ these engineered tandem electrodes in cells with cross-over mitigation strategies (for example, BPMs, acidic electrolytes) to further enhance single-pass conversion of the fed CO_2.

Conclusions

Tandem catalysts designed to convert CO_2 into C_{2+} products must efficiently manage the CO intermediate to achieve high FE for C_{2+} at high j_{C2+}. In this work, we designed a simple yet efficient s-GDE in which a short, heavily loaded CO-selective CL segment placed at the inlet of the s-GDE prolongs the residence time of generated CO in the subsequent Cu CL segment where C–C coupling takes place. By optimizing the relative lengths and loadings of Cu and Ag in a Cu/Ag s-GDE, we maximized the residence time of CO in the Cu CL segment to facilitate a 300% increase in CO utilization compared to a non-segmented Cu/Ag GDE. Moreover, we found that a 250% increase in j_{C2+} relative to pure Cu could be achieved using an optimized Cu:Ag area ratio of 1.00:0.05. A 2D continuum model verified the effects of CL area ratios, residence time and feed flow rate on the θ_{*CO} on the observed enhancements in j_{C2+}. Lastly, using the s-GDE design and a Cu/Fe-N-C tandem CL, 90% FE to C_{2+} products at a j_{C2+} exceeding 1 A cm^{-2} and a half-cell energy efficiency for CO_2-to-C_2H_4 conversion of 40.1% was achieved. The s-GDE architecture employed in the present study presents unique opportunities for application in industrial systems for CO_2 electrolysis. Aside from the achievement of high C_{2+} current densities and FEs with a relatively low loading of Ag, the present study leverages along-the-channel gradients to enhance CO utilization in a tandem catalyst. These downstream concentration gradients will be more pronounced in industrial systems that employ larger electrodes for CO_2 reduction at scale. Therefore, it can be imagined that the

developed s-GDE scheme would be even more effective at scale, and future studies should aim to examine the performance of these s-GDEs within industrial-scale electrolysers, cell sizes, and distinct flow-channel architectures to enhance the readiness of the emerging technology.

Methods

Multiphysics simulation. The simulation was performed using the COMSOL Multiphysics v.5.6 software package. The Navier–Stokes equations were used to solve the bulk fluid transport within the flow channel. Darcy's law described the flow of fluid through a porous medium. The concentration of species was solved throughout the domain by solving species conservation and the θ_{*CO} was defined by the Langmuir adsorption model. Supplementary Methods provide more detailed information regarding the simulations.

Preparation of the segmented gas-diffusion electrode. The Cu catalyst ink was prepared by dispersing 200 mg of Cu nanoparticles (25 nm, Millipore Sigma) in a solvent mixture, followed by ultrasonication for 30 minutes. The solvent mixture was composed of 20 ml water, 20 ml isopropyl alcohol and 500 µl Sustainion XA-9 ionomer solution (5 wt%). The Ag (20–40 nm, Alfa Aesar), ZnO (<100 nm, Millipore Sigma) and Fe-N-C catalyst inks were prepared using the same procedure. The volume of solvent and ionomer solution was adjusted in proportion to the catalyst weight. The Cu catalyst ink was first sprayed onto the 8.0 × 25.0 cm^2 gas-diffusion layer (GDL, Sigracet 39BC) to fabricate a uniform Cu GDE. The actual loading of Cu catalyst was 0.40 mg cm^{-2} unless otherwise stated. The catalyst loading was determined by weighing the electrode before and after the spraying. This Cu GDE was then cut into four equal pieces (2.0 × 25.0 cm^2). Three of them were used for subsequent coating with CO-selective catalyst inks, while the fourth piece was used as a control electrode.

The Cu GDE was then covered by various templates made of polyethylene terephthalate plastic. The templates were machined to open windows with different lengths of 0.10, 0.20, 0.40, 0.80, 1.20, 1.60 and 1.90 cm. Afterwards, the Ag catalyst ink was sprayed onto the Cu CL to form an Ag CL segment with a constrained area at one end of the electrode. The mass of Ag catalyst was fixed to 0.04 mg for each 1.0 cm^2 stacked s-GDE. The quantity was determined by weighing a large piece of the electrode before and after the spraying. The templates with lengths of 1.0 mm and 19.0 mm were used together to fabricate the coplanar Cu/Ag s-GDE. The mass of Cu and Ag catalyst in each 1.0 cm^2 coplanar Cu/Ag s-GDE was also 0.40 and 0.04 mg, respectively. Following spraying, the s-GDEs were dried at 60 °C in the vacuum oven. Finally, the big sheet of stacked s-GDE was cut into smaller samples with dimensions of 2.00 cm (length, L) × 0.50 cm (width, W) corresponding to an area of 1.00 cm^2 for the electrochemical tests. For the coplanar Cu/Ag s-GDE, the Cu and Ag CLs had the same width of 0.50 cm, and the segment areas were 0.95 and 0.05 cm^2 for Cu and Ag CLs, respectively. The Cu/Ag (1.00:1.00) s-GDE, which has an equal area of 1.00 cm^2 for Cu and Ag CLs segments, was equivalent to the l-GDE. The Cu/ZnO and Cu/Fe-N-C s-GDEs were fabricated by following the same procedure. The doubly loaded Cu/Fe-N-C s-GDE contained a Cu loading of 0.80 mg cm^{-2} and Fe-N-C mass of around 0.08 mg for each 1.0 cm^2 electrode.

Preparation of modified s-GDEs. To prepare the modified s-GDEs, the uniform Cu CL (0.40 mg cm^{-2}) segment (2.00 × 0.50 cm^2) was first coated onto the GDL, followed by a condensed Ag CL segment (0.20 (L) × 0.50 (W) cm^2) at the inlet. The amount of Ag catalyst (0.04 mg for each 1.0 cm^2 electrode) was kept the same for all electrodes. The area and position of the Ag CL segment were precisely controlled by a machined template. Afterwards, a subsegment of the Cu CL with length varying from 0 to 1.80 cm was exfoliated off the GDL by 3M Magic tape until the microporous layer of black carbon was entirely exposed. The exposed GDL was then sealed by epoxy to prevent the undesired hydrogen evolution reaction from occurring on the carbon (Supplementary Fig. 31). The backside of the exposed carbon paper was sealed as well to prevent the gas from diffusing into the carbon paper in the exfoliated area.

Preparation of Fe-N-C catalyst. The Fe-N-C catalyst was synthesized according to our previous report[47]. Briefly, 1 g of the PBX 51 powder (Cabot) was oxidized by the oxygen plasma and then dispersed in 100 ml of 5 mg ml^{-1} ferric chloride hexahydrate (Millipore Sigma) solution. After sonicating for 2 h, followed by stirring for 12 h, the precipitate was collected by centrifuging and was dried in the oven overnight. Next, 100 mg of the carbon substrate was ground together with 300 mg of dicyandiamide and pyrolyzed in the tube furnace at 650 °C for 2 h under the N_2 stream. The obtained black powder was then washed in 1 M HNO_3 for 12 h. Finally, after drying the powder in the oven overnight, the Fe-N-C catalyst was ready to use.

Electrode characterization. The cross-sectional area of the electrode was imaged by SEM (FEI SCIOS DualBeam). The SEM samples were prepared by breaking the electrodes in the liquid N_2. The optical images of electrodes were taken by optical microscopes (Keyence VHX-2000E).

The electrochemically active surface area was determined by measuring the double-layer capacitance (C_{dl}) of the corresponding electrodes in Ar-purged 1.0 M KOH in an H-type electrolyser. To exclude the effect of carbon paper, the backside of the electrode was sealed with epoxy and only left the CL exposed. The scan rate varied from 10 to 100 mV s^{-1} in the non-Faradaic potential range. The obtained current was plotted as a function of the scan rate to derive the C_{dl}.

CO_2 electrochemical reduction in the MEA electrolyser. The activity and selectivity of both s-GDE and l-GDE were tested in a customized MEA electrolyser comprising the GDE cathode, Sustainion anion-exchange membrane and the Ni-Fe LDH coated Ni foam as the anode. The 0.50 M KOH or 0.10 M $KHCO_3$ anolyte stream that flowed through the anode at a rate of 5.00 ml min^{-1} was controlled by a peristaltic pump (Harvard Apparatus P70-7000). The dry CO_2 feedstock was supplied to the cathode at a rate of 20 standard cubic centimetres per minute (sccm) controlled by a mass flow controller (Alicat Scientific MC-100SCCM-D). The applied cell voltage was controlled by a potentiostatic/galvanostatic station (Solartron EnergyLab XM). The anode potential was monitored online in reference to a saturated calomel electrode. The gas products were quantified by gas chromatography (GC, Agilent 7890B), while liquid products were measured by ^{1}H NMR spectroscopy (Bruker AV500).

The FE of each gas product was calculated on the basis of a previous equation where the outlet CO_2 flow rate was accurately measured[29]. For the measurement of outlet CO_2 flow rate, a constant stream of Ar gas (10 sccm) was used as an internal reference and evenly mixed with the cell outlet gas stream before it was injected into the GC column. The standard curve for CO_2 flow rate was established by a similar way of mixing the 10 sccm Ar gas with a pure CO_2 stream with a flow rate varying from 5 to 100 sccm. The concentration of other gas components was quantified by using CO_2 as the internal reference. The standard GC calibration curves for the other gas components were established based on three standard calibration gases, comprising 1,000, 2,000 and 5,000 ppm of H_2, CO, CH_4, C_2H_4 and C_2H_6, respectively, with CO_2 as the balance gas.

The internal ohmic resistance between the cathode and anode was determined by electrochemical impedance spectroscopy operated under open-circuit voltage with a frequency ranging from 10^5 Hz to 0.01 Hz. Almost 90% of the measured cell resistances ranged from 0.20 to 0.30 Ω, while around 10% of cell resistance ranged from 0.50 to 0.60 Ω. Contact resistances resulting from cell assembly contributed 0.10 Ω variance, whereas variations in the membrane ion conductivity from batch to batch accounted for another 0.30 Ω variance. Therefore, to deconvolute the impacts of these variances from the kinetic performance, the cell voltage was IR compensated unless otherwise stated. All the reported cell voltages were corrected by the measured cell internal resistance loss under each specific test unless otherwise stated. For the modified s-GDEs, the cathode potential was obtained by subtracting the recorded anode potential from the IR-free cell voltage.

The full-cell energy efficiency for a specific product i was assessed according to

$$\mathrm{EE}_{i,\mathrm{full-cell}}(\%) = \frac{E_i^0}{V_{\mathrm{cell}}} \times \mathrm{FE}_i(\%) \quad (1)$$

where E_i^0 is the equilibrium cell voltage ($E_i^0 = E_{\mathrm{anode}}^0 - E_{i,\mathrm{cathode}}^0$) for a specific product i; V_{cell} is the applied cell voltage; FE_i is the Faradaic efficiency of product i.

The half-cell energy efficiency for a specific product i was calculated by the following equation:

$$\mathrm{EE}_{i,\mathrm{half-cell}}(\%) = \frac{E_i^0}{E_{\mathrm{anode}}^0 - E_{\mathrm{cathode}}} \times \mathrm{FE}_i(\%) \quad (2)$$

where E_{cathode} is the applied cathode potential.

CO_2 reduction in the flow cell. The flow cell, including a 2 mm buffer layer of catholyte (0.5 M KOH), has a larger ohmic resistance (1.00 to 1.10 Ω) than that for the MEA electrolyser. The test conditions in the flow cell were generally identical to those in the MEA electrolyser except that a catholyte was supplied at a flow rate of 0.5 ml min^{-1}.

Long-term stability test in the MEA electrolyser and flow cell. The long-term stability was operated under potentiostatic mode in which the cell voltage was controlled by the Solartron EnergyLab XM. During the long-term testing, gas and liquid products were periodically quantified by GC and ^{1}H NMR, respectively.

Calculation of the CO_2 reduction performance on each subsegment. The Cu CL subsegment (S_i) as shown in Fig. 3e was defined as the difference in Cu CL segments between two consecutive modified s-GDEs (E_i) as follows:

$$S_1 = E_1 \quad (3)$$

$$S_i = E_i - E_{i-1}, (6 \geq i \geq 2) \quad (4)$$

where i is an integer. Correspondingly, the $j_{C_{2+}}$ for each subsegment was calculated by finding the total current in each subsegment and dividing by the subsegment area as follows:

$$j_{C_{2+}}(S_1) = \frac{I_{C_{2+}}(E_1)}{A(E_1)} \quad (5)$$

$$j_{C_{2+}}(S_i) = \frac{I_{C_{2+}}(E_i) - I_{C_{2+}}(E_{i-1})}{A(E_i) - A(E_{i-1})},\ (6 \geq i \geq 2) \quad (6)$$

In this equation, $I_{C_{2+}}(E_i)$ is the total C_{2+} current (units of mA) in segment E_i, $A(E_i)$ is the area of segment E_i and $j_{C_{2+}}(S_i)$ is the C_{2+} current density (units of mA cm^{-2}) in subsegment S_i.

Calculation of the outlet CO flow rate from each subsegment. The outlet CO flow rate for each S_i was directly converted from the I_{CO} for the corresponding E_i according to the following equation:

$$Q_{CO}(S_i) = \frac{I_{CO}(E_i)}{nF} \quad (7)$$

where the Q_{CO} (mol s^{-1}) represents the flow rate of CO along the y axis of the electrode within a given subsegment, n is the number of electron transfers ($n=2$) and F is Faraday's constant.

Calculation of CO_2 cross-over. This work applied an Ar stream with a constant flow rate as an internal standard to calibrate the CO_2 flow rate; so that the CO_2 flow rate at the outlet can be accurately measured, as shown below.

$$\frac{Q_{CO_2}}{Q_{Ar}} = a \times \frac{A_{CO_2}}{A_{Ar}} + b \quad (8)$$

where the Q_{CO_2} and Q_{Ar} are the volumetric flow rate of CO_2 and Ar, while the Q_{Ar} is 10.00 sccm; A_{CO_2} and A_{Ar} represent the peak area of CO_2 and Ar in the GC trace; and a and b are the slope and intercept of the calibration curve, respectively.

The difference in CO_2 flow rate between the inlet and outlet accounts for the CO_2 consumption and the CO_2 cross-over to the anode side. The volumetric rate of CO_2 ($\dot{V}$) consumed by the Faradaic reaction can be calculated from the current.

$$\dot{V}_{consumption} = \frac{\sum \frac{I_i}{n_i * F} \times R \times T}{P} \quad (9)$$

where n is the number of charge transfers for product i; F is the Faradaic constant; R is the gas constant; P is the gas pressure; and T is the temperature.

Therefore, the volume of CO_2 cross-over can be calculated as follows.

$$\dot{V}_{crossover} = \dot{V}_{inlet} - \dot{V}_{outlet} - \dot{V}_{consumption} \quad (10)$$

Data availability

Source data are provided with this paper. All data generated and analysed during the present study are available from the authors upon reasonable request.

Received: 15 July 2021; Accepted: 20 January 2022;
Published online: 03 March 2022

References

1. Jouny, M., Luc, W. W. & Jiao, F. A general techno-economic analysis of CO_2 electrolysis systems. *Ind. Eng. Chem. Res.* **57**, 2165–2177 (2018).
2. Nitopi, S. et al. Progress and perspectives of electrochemical CO_2 reduction on copper in aqueous electrolyte. *Chem. Rev.* **119**, 7610–7672 (2019).
3. Dinh, C.-T. et al. CO_2 electroreduction to ethylene via hydroxide-mediated copper catalysis at an abrupt interface. *Science* **360**, 783–787 (2018).
4. Gao, Y. et al. Recent advances in intensified ethylene production—a review. *ACS Catal.* **9**, 8592–8621 (2019).
5. Montoya, J. H., Peterson, A. A. & Nørskov, J. K. Insights into C-C coupling in CO_2 electroreduction on copper electrodes. *ChemCatChem* **5**, 737–742 (2013).
6. Montoya, J. H., Shi, C., Chan, K. & Norskov, J. K. Theoretical insights into a CO dimerization mechanism in CO_2 electroreduction. *J. Phys. Chem. Lett.* **6**, 2032–2037 (2015).
7. Schouten, K. J. P., Kwon, Y., van der Ham, C. J. M., Qin, Z. & Koper, M. T. M. A new mechanism for the selectivity to C_1 and C_2 species in the electrochemical reduction of carbon dioxide on copper electrodes. *Chem. Sci.* **2**, 1902–1909 (2011).
8. Schouten, K. J. P., Pérez Gallent, E. & Koper, M. T. M. Structure sensitivity of the electrochemical reduction of carbon monoxide on copper single crystals. *ACS Catal.* **3**, 1292–1295 (2013).
9. Liu, X. et al. pH effects on the electrochemical reduction of CO_2 towards C_2 products on stepped copper. *Nat. Commun.* **10**, 32 (2019).
10. Garza, A. J., Bell, A. T. & Head-Gordon, M. Mechanism of CO_2 reduction at copper surfaces: pathways to C_2 products. *ACS Catal.* **8**, 1490–1499 (2018).
11. Resasco, J. et al. Promoter effects of alkali metal cations on the electrochemical reduction of carbon dioxide. *J. Am. Chem. Soc.* **139**, 11277–11287 (2017).
12. Li, J. et al. Constraining CO coverage on copper promotes high-efficiency ethylene electroproduction. *Nat. Catal.* **2**, 1124–1131 (2019).
13. Choi, C. et al. Highly active and stable stepped Cu surface for enhanced electrochemical CO_2 reduction to C_2H_4. *Nat. Catal.* **3**, 804–812 (2020).
14. Gu, Z. et al. Efficient electrocatalytic CO_2 reduction to C_{2+} alcohols at defect-site-rich Cu surface. *Joule* **5**, 429–440 (2021).
15. Zhong, M. et al. Accelerated discovery of CO_2 electrocatalysts using active machine learning. *Nature* **581**, 178–183 (2020).
16. Vasileff, A., Xu, C., Jiao, Y., Zheng, Y. & Qiao, S.-Z. Surface and interface engineering in copper-based bimetallic materials for selective CO_2 electroreduction. *Chem* **4**, 1809–1831 (2018).
17. Huang, Y., Handoko, A. D., Hirunsit, P. & Yeo, B. S. Electrochemical reduction of CO_2 using copper single-crystal surfaces: effects of CO* coverage on the selective formation of ethylene. *ACS Catal.* **7**, 1749–1756 (2017).
18. Monzó, J. et al. Enhanced electrocatalytic activity of Au@Cu core-shell nanoparticles towards CO_2 reduction. *J. Mater. Chem. A* **3**, 23690–23698 (2015).
19. Morales-Guio, C. G. et al. Improved CO_2 reduction activity towards C_{2+} alcohols on a tandem gold on copper electrocatalyst. *Nat. Catal.* **1**, 764–771 (2018).
20. Chen, C. et al. Cu-Ag tandem catalysts for high-rate CO_2 electrolysis toward multicarbons. *Joule* **4**, 1688–1699 (2020).
21. Wang, X. et al. Mechanistic reaction pathways of enhanced ethylene yields during electroreduction of CO_2–CO co-feeds on Cu and Cu-tandem electrocatalysts. *Nat. Nanotechnol.* **14**, 1063–1070 (2019).
22. Gao, J. et al. Selective C-C coupling in carbon dioxide electroreduction via efficient spillover of intermediates as supported by operando Raman spectroscopy. *J. Am. Chem. Soc.* **141**, 18704–18714 (2019).
23. Fu, J. et al. Bipyridine-assisted assembly of Au nanoparticles on Cu nanowires to enhance electrochemical reduction of CO_2. *Angew. Chem. Int. Ed. Engl.* **131**, 14238–14241 (2019).
24. Hoang, T. T. H. et al. Nanoporous copper-silver alloys by additive-controlled electrodeposition for the selective electroreduction of CO_2 to ethylene and ethanol. *J. Am. Chem. Soc.* **140**, 5791–5797 (2018).
25. Li, F. et al. Cooperative CO_2-to-ethanol conversion via enriched intermediates at molecule–metal catalyst interfaces. *Nat. Catal.* **3**, 75–82 (2019).
26. Wang, L. et al. Electrochemical carbon monoxide reduction on polycrystalline copper: effects of potential, pressure, and pH on selectivity toward multicarbon and oxygenated products. *ACS Catal.* **8**, 7445–7454 (2018).
27. Schreier, M., Yoon, Y., Jackson, M. N. & Surendranath, Y. Competition between H and CO for active sites governs copper-mediated electrosynthesis of hydrocarbon fuels. *Angew. Chem. Int. Ed. Engl.* **57**, 10221–10225 (2018).
28. Ren, D. et al. Atomic layer deposition of ZnO on CuO enables selective and efficient electroreduction of carbon dioxide to liquid fuels. *Angew. Chem. Int. Ed. Engl.* **58**, 15036–15040 (2019).
29. She, X. et al. Tandem electrodes for carbon dioxide reduction into C_{2+} products at simultaneously high production efficiency and rate. *Cell Rep. Phys. Sci.* **1**, 100051 (2020).
30. Zhang, T., Li, Z., Zhang, J. & Wu, J. Enhance CO_2-to-C_{2+} products yield through spatial management of CO transport in Cu/ZnO tandem electrodes. *J. Catal.* **387**, 163–169 (2020).
31. Levenspiel, O. *Chemical Reaction Engineering* 3rd edn, Ch. 5 (John Wiley & Sons, 1999).
32. Weng, L.-C., Bell, A. T. & Weber, A. Z. A systematic analysis of Cu-based membrane-electrode assemblies for CO_2 reduction through multiphysics simulation. *Energy Environ. Sci.* **13**, 3592–3606 (2020).
33. Kas, R. et al. Along the channel gradients impact on the spatioactivity of gas diffusion electrodes at high conversions during CO_2 electroreduction. *ACS Sustain. Chem. Eng.* **9**, 1286–1296 (2021).
34. Bui, J. C., Kim, C., Weber, A. Z. & Bell, A. T. Dynamic boundary layer simulation of pulsed CO_2 electrolysis on a copper catalyst. *ACS Energy Lett.* **6**, 1181–1188 (2021).
35. Dunwell, M., Luc, W., Yan, Y., Jiao, F. & Xu, B. Understanding surface-mediated electrochemical reactions: CO_2 reduction and beyond. *ACS Catal.* **8**, 8121–8129 (2018).
36. Moradzaman, M., Martínez, C. S. & Mul, G. Effect of partial pressure on product selectivity in Cu-catalyzed electrochemical reduction of CO_2. *Sustain. Energy Fuels* **4**, 5195–5202 (2020).
37. Hori, Y., Takahashi, R., Yoshinami, Y. & Murata, A. Electrochemical reduction of CO at a copper electrode. *J. Phys. Chem. B* **101**, 7075–7081 (1997).
38. Wang, L. et al. Selective reduction of CO to acetaldehyde with CuAg electrocatalysts. *Proc. Natl Acad. Sci. USA* **117**, 12572–12575 (2020).

39. Corral, D. et al. Advanced manufacturing for electrosynthesis of fuels and chemicals from CO_2. *Energy Environ. Sci.* **14**, 3064–3074 (2021).
40. Tan, Y. C., Lee, K. B., Song, H. & Oh, J. Modulating local CO_2 concentration as a general strategy for enhancing C–C coupling in CO_2 electroreduction. *Joule* **4**, 1104–1120 (2020).
41. Salvatore, D. A. et al. Electrolysis of gaseous CO_2 to CO in a flow cell with a bipolar membrane. *ACS Energy Lett.* **3**, 149–154 (2017).
42. Chen, Y. et al. A robust, scalable platform for the electrochemical conversion of CO_2 to formate: identifying pathways to higher energy efficiencies. *ACS Energy Lett.* **5**, 1825–1833 (2020).
43. Huang, J. E. et al. CO_2 electrolysis to multicarbon products in strong acid. *Science* **372**, 1074–1078 (2021).
44. McCallum, C. et al. Reducing the crossover of carbonate and liquid products during carbon dioxide electroreduction. *Cell Rep. Phys. Sci.* **2**, 100522 (2021).
45. Li, T. et al. Electrolytic conversion of bicarbonate into CO in a flow cell. *Joule* **3**, 1487–1497 (2019).
46. Weng, L.-C., Bell, A. T. & Weber, A. Z. Towards membrane-electrode assembly systems for CO_2 reduction: a modeling study. *Energy Environ. Sci.* **12**, 1950–1968 (2019).
47. Zhang, T. et al. Nickel-nitrogen-carbon molecular catalysts for high rate CO_2 electro-reduction to CO: on the role of carbon substrate and reaction chemistry. *ACS Appl. Energy Mater.* **3**, 1617–1626 (2020).

Acknowledgements

This material is based upon work supported by the Office of Fossil Energy and Carbon Management of the US Department of Energy under award number DE-FE0031919 and performed at the Joint Center for Artificial Photosynthesis, a DOE Energy Innovation Hub, supported through the Office of Science of the US Department of Energy under award number DE-SC0004993 and the National Institutes of Health under grant no. S10OD023532. The authors at University of Cincinnati also thank National Science Foundation for financial support (award no. CBET-2033343). J.C.B. acknowledges funding from the National Science Foundation Graduate Research Fellowship under grant no. DGE 1752814. J.C.B. acknowledges funding, in part, by a fellowship award through the National Defense Science and Engineering Graduate (NDSEG) Fellowship Program sponsored by the Army Research Office (ARO). J.C.B. would also like to acknowledge fruitful discussion regarding along-the-channel transport in CO_2 electrolysers with E. Lees.

Author contributions

J.W., A.Z.W. and A.T.B. supervised the project. J.W. and T.Z. designed the experiments. T.Z. prepared the electrodes, performed electrochemical experiments and characterizations with the help of Z.L. J.C.B. performed multiphysics simulation. T.Z., Z.L. and J.C.B. performed data interpretation. T.Z., J.C.B., A.T.B., A.Z.W. and J.W. wrote the manuscript. All authors discussed, commented on and revised the manuscript.

Competing interests

The authors declare no competing interests.

Additional information

Supplementary information The online version contains supplementary material available at https://doi.org/10.1038/s41929-022-00751-0.

Correspondence and requests for materials should be addressed to Adam Z. Weber or Jingjie Wu.

Peer review information *Nature Catalysis* thanks Edward Anthony and the other, anonymous, reviewer(s) for their contribution to the peer review of this work.